Observation-driven model for calculating water harvesting potential from advective fog in (semi-)arid coastal regions

Felipe Lobos-Roco[1,2], Jordi Vilà-Guerau de Arellano[3], and Camilo del Río[4]

[1]Centro UC Desierto de Atacama, Pontificia Universidad Católica de Chile.
[2]Facultad de Agronomía y Sistemas Naturales, Pontificia Universidad Católica de Chile.
[3]Meteorology and Air Quality group, Wageningen University, the Netherlands.
[4]Instituto de Geografía, Pontificia Universidad Católica de Chile.

Correspondence: Felipe Lobos-Roco (flobosr@uc.cl; felipe.lobos.roco@gmail.com)

Abstract.

Motivated by finding complementary water sources in (semi-)arid regions, we develop and assess an observational-driven model to calculate fog harvesting water potential. We aim to integrate this model with routine meteorological data collected under complex meteorological and topographic conditions to characterize the advective fog phenomenon. Based on the mass balance principle, the **A**dvective fog **M**odel for (semi-)**A**rid **R**egions **U**nder climate change (AMARU) offers insights into fog water harvesting volumes in time and space domains. The model is based on a simple thermodynamic approach to calculate the dependence of the liquid water content ($\frac{q_t}{r_l}$) on height. Based on climatological fog collection records, we introduce an empirical efficiency coefficient. When combined with $\frac{q_t}{r_l}$, this coefficient facilitates the estimation of fog harvesting volumes (L m^{-2}). AMARU's outputs are validated against in-situ observations collected over Chile's coastal (semi-)arid regions at various elevations and years (2018-2023). The model's representations of the seasonal cycle of fog harvesting follow observations with errors of ~10%. The model satisfactorily estimates the maximum $\frac{q_t}{r_l}$ (~0.8 g kg^{-1}) available for fog harvesting potential in the vertical column. To assess spatial variability, we combine the model with satellite-retrieved data, enabling the mapping of fog harvesting potential along the Atacama coast. Our approach enables the application of the combined observational-AMARU model to other (semi-)arid regions worldwide that share similar conditions. Through the quantification of fog harvesting, our model contributes to water planning, ecosystem delimitation efforts, and the study of the climatological evolution of cloud water, among others.

1 Introduction

Water resources in (semi-)arid regions are of critical value for social, economic, and ecological development. However, in recent decades, climate change has enhanced drought periods, intensifying water stress in areas already facing scarcity. This has resulted in a worldwide dryland expansion (Koppa et al., 2023). For example, Chile's (semi-)arid and mediterranean regions have suffered a fifteen-year drought, experiencing a nearly 40% decrease in precipitation (Garreaud et al., 2021). Likewise, other dry regions such as California, South Africa, Australia, Spain, and Morocco are confronting similar challenges related to water scarcity, including new threats like fire risks, degradation of soil ecosystems, and impacts on food security (Goulden and

Bales, 2019; Berbel and Esteban, 2019; Keeley and Syphard, 2021; Kogan and Kogan, 2019). Moreover, future IPCC's climate
25   scenarios are discouraging, projecting even drier conditions by 2050 (Masson-Delmotte et al., 2021). Under this escalating
water scarcity scenario, the exploration of new water resources is imperative.

In this context, the collection of freshwater from fog presents itself as a viable alternative to face water scarcity, especially in
(semi-)arid regions along the subtropical western coasts. Fog harvesting has long represented a significant untapped water po-
30   tential in the world's dry regions (Klemm et al., 2012). For example, in the coastal Atacama Desert, fog and dew represent the
sole water source across vast territories with almost null precipitations (Cereceda et al., 2008). However, quantifying this water
potential represents a scientific challenge, requiring a deep understanding of the physical processes controlling the formation
and dissipation of the marine stratocumulus (Sc) cloud deck over the ocean (Andersen et al., 2020; del Río et al., 2021b),
its interaction with coastal topography (Lobos-Roco et al., 2018), and the effectiveness of fog collector designs (Verbrugghe
35   and Khan, 2023). In addition, the lack of available and direct observations of the fog phenomenon, combined with the com-
plexity of topography, makes it challenging to pinpoint where fog forms, identify optimal harvesting seasons, and determine
potential yield. Consequently, advancing our knowledge to quantify harvestable water from fog clouds is imperative to develop
this promising alternative water source. Estimating where, when, and how much water can be harvested from fog is socially
relevant. Estimating fog water potential can facilitate the transition from experimental fog harvesting practices to industrial
40   ones (Lobos-Roco et al., 2024), potentially enhancing the development of overlooked desert territories, and benfiting their
local communities. Moreover, estimating potential fog water production can help us better understand the unique ecosystems
sustained by fog (Koch et al., 2019; Muñoz-Schick et al., 2001; Moat et al., 2021), contributing to the assessment of their
conservation status under a rapidly warming climate.

45   Fog is a meteorological phenomenon defined by a boundary layer cloud in permanent contact with the Earth's surface (Roach,
1995; Stull, 2012). The origins of fog are, influenced by different atmospheric boundary layer and local topographic conditions.
However, in most of the (semi-)arid regions along the (sub)tropical western margins of continents, fog formation is driven by the
ocean to land advection of the Sc cloud. The Sc cloud forms over the ocean in a vast deck ~~influenced by~~ controlled by a strong
inversion layer resulted from the interaction between the sea surface temperature and large-scale subsidence ~~(Wood, 2012)~~
50   ~~, whose interaction results in a strong thermal inversion layer (Muñoz et al., 2011). The~~ (Muñoz et al., 2011). Here, one of
the main physical involved in stratocumulus formation is the microphysical properties of cloud droplets, which are linked to
cloud optical properties that have important climate effects (Wood, 2012). In the South East Pacific, cloud droplet sizes of 5
to 15 μm are often found, whose concentration is ~~$\leq$50 cm^{-3}~~ 50 cm^{-3} increasing to 200 cm^{-3} along coastal areas of Chile
(Painemal and Zuidema, 2011). The droplet size and concentration determines the liquid water content (Gultepe et al., 2021)
55   , which essentially is the amount of water that can be harvested on land once Sc becomes fog. As well as, the stability of the
marine boundary layer (MBL) determines the formation, maintenance, and dissipation of the Sc cloud. Formation and main-
tenance depend on how well-mixed (<3.1 x 10^{-3} K m^{-1}) the MBL is, while the dissipation is influenced by its stratification
(>3.1 x 10^{-3} K m^{-1}) (Lobos-Roco et al., 2018). This cloud forms at the upper part of the MBL, exhibiting a clear vertical

structure. This structure is characterized by an averaged cloud base ranging from 300 to 400 m (Lu et al., 2007), determined by the lifting condensation level. As the latter increases, the liquid water content progressively rises, peaking at the cloud top ($\sim$0.7 g kg^{-1}) (Schween et al., 2022). The liquid water content abruptly drops to 0 g kg^{-1} just above the cloud top, where the air becomes stratified and extremely dry. The Sc cloud is advected into the continent by the typical strong thermal-driven sea breeze of (semi-)arid regions (Lobos-Roco et al., 2021). Upon reaching land, the cloud deck is affected by local conditions that, together with the high topography, lift it, forming fog belts (del Río et al., 2021b). Depending on latitude and topography, these fog belts vary in altitude; for example, in the Atacama region, they are found in the coastal mountains between 600 to 1200 m ASL (Cereceda et al., 2008; Garreaud et al., 2008). This narrow belt represents the area where fog can potentially be harvested.~~This~~

~~The~~ harvesting process is ~~already~~ made by nature through specialized plants that accumulate water in their leaves, spines, and branches, making it available for the soil and roots (Malik et al., 2014; García et al., 2021; Koch et al., 2019). ~~Likewise, artificial collectorshave been developed to~~ However, fog can also be harvested artificially through passive collectors, which efficiently harvest fog water using meshes (Schemenauer and Cereceda, 1994). Numerous studies have reported promising fog harvesting volumes worldwide in arid and semi-arid regions. For example, rates between 6-8 L m^{-2} d^{-1} have been reported in the hyperarid Atacama Desert in Chile (Cereceda et al., 2002; Larrain et al., 2002), 1-5 L m^{-2} d^{-1} along the western coast of South Africa (Klemm et al., 2012), and 7 L m^{-2} d^{-1} in the Iberian Peninsula, Spain (Estrela et al., 2009).

In recent years, significant progress has been achieved in understanding the spatial variability of Sc cloud and fog (del Río et al., 2021b; Andersen et al., 2020), as well as the vertical structure of the fog cloud (García et al., 2021; Lobos-Roco et al., 2018) and the practical applications of fog and dew collection in water-stressed regions (Lobos-Roco et al., 2024; Baguskas et al., 2021). Despite these advancements, there remains a need to integrate these findings into a unified model that can address the questions of where, when, and how much water can be harvested from clouds. In this research, we present the **A**dvective fog **M**odel for (semi-)**A**rid **R**egions **U**nder climate change (AMARU), a phenomenological model designed to estimate fog harvesting potential volumes continuously in time and space.

2   Model formulation and evaluation

The AMARU aims to estimate ~~the liquid water capacity~~ in a simple way the adiabatic liquid water content of Sc clouds and the potential for fog harvesting~~using widely~~. Our goal is to design a model that use the available routine meteorological ~~data. Based on phenomenological principles, Figure 1 schematizes the physical interpretation, including all variables, dimensions, and processes~~ observations in an area with significant ocean-land contrasts and very complex topography. Figure 1 shows the physical assumptions and processes along with the respective variables and units. The model ~~relies on~~ is derived from the mass conservation ~~principle in dimensional analysis. When fog occurs~~equation. The sequence of physical mechanisms are: (i) during a fog event, a certain amount of ~~water~~ liquid water (W_h) is retained from the total ~~specific humidity (q) that passes~~ fog inflow

when passing through a passive collector. ~~This implies~~ We assume that the harvested fog water results from the difference between ~~water input and water output~~ fog inflow (F_{in}) and outflow (F_{out}) in g kg^{-1} m s^{-1}. This equation reads as follows ~~:~~

$$\frac{dq_h}{dt} \simeq \frac{\Delta q_h}{\Delta t} W_h = q F_{in} - q F_{out},\tag{1}$$

95 ~~here, q_h is the fog harvesting capacity, q_{in} is the total humidity available in the air for harvesting by the collector, and q_{out} is~~ (ii) Fog inflow and outflow are described as fluxes of the mixing ratio:

$$F_{in} = r_l u_x,\tag{2}$$

$$F_{out} = F_{in}(1 - \eta),\tag{3}$$

where r_l is the liquid water mixing ratio, defined as the amount of ~~humidity that remains unharvested. We introduce three~~
100 ~~assumptions: (1) the total specific humidity corresponds to the sum of saturated specific humidity and air-liquid water content, expressed as $q = q_s + q_l$; (2) given that q_l is by two orders of magnitude lower than q_s, we approximated $q_{s(in)} \simeq q_{s(out)}$; (3) $q_{in} > q_{out} > q_h$.~~ liquid water (m_l in Fig.1) per unit mass of dry air (m_d) that contains it, expressed in grams of water per kilograms of dry air. To calculate the inflow we use u_x, which represents the perpendicular (mean $\pm$ std) wind speed (m s^{-1}) relative to the collector. (iii) The term η is a dimensionless ration representing the collector efficiency. This coefficient is
105 described as:

~~With these assumptions, we define the water input as the amount of liquid water present in the air (q_l), while q_h is a fraction of this total water input. To combine the model with routine observations~~

$$\eta = \frac{W_h}{F_{in}},\tag{4}$$

where η corresponds to the percentage of water harvested over the total water that can potentially pass through the collector
110 (calculation in Section 2.2). Reordering the terms, we express Equation (1) in net terms as:

$$\frac{dq_h}{dt} W_h = r_l u q_l A_x \eta,.\tag{5}$$

The W_h units are then g kg^{-1} m s^{-1}. However, in giving the final output, we convert L m^{-2}s^{-1} (equivalent to mm) once grams are transformed to liters and dry air density (kg m^{-3}) is included as:

$$W_h = r_l \rho_a u_x \eta. \tag{6}$$

115 Finally, W_h is integrated over a period as:

$$\overline{W}_h^{\Delta t} = \int_{t_0}^{t_1} W_h dt \tag{7}$$

where t_0 and t_1 correspond to the initial and ending times. The model has three main assumptions described as follows: (1) ~~to~~ $F_{in} > F_{out}$; (2) ~~can be found in Appendix A~~ since the model aims to reproduce advective fog collection, it is assumed that condensation only occurs in the atmosphere under the conditions $r_l = r_v - r_s$; (3) the mixing ratio (r_v) being two orders of

120 magnitude higher than r_l, is nearly conserved.

In Equation (~~2), two terms are particularly sensitive: q_t~~ 6), r_l and η ~~. The former~~ depend on location and condensation processes. Regarding location, r_l varies in height (the vertical dimension of the model) and depends on the conditions of the marine Sc cloud over the ocean and its interaction with the topography. To estimate this variable using routine data, we assume that water vapor condenses once it reaches the thermodynamic conditions to reach saturation. This assumption implies that we

125 do not take microphysical properties such droplet size, nucleation or droplet concentration into the calculations. The second term, η ~~is related to~~ groups cloud microphysics, ~~as well as the design and material properties of the collector~~ the collector design, and its material properties. To delve into the ~~details of q_t~~ detailed calculation of r_l and η, we ~~deconstruct Equation (2~~ break down the analysis of Equation (6) into two parts: the thermodynamic and water potential modules ~~. Additionally, to study the model's horizontal spatial variability~~ (section 2.1 and 2.2). In addition, we introduce a third module ~~in this section,~~

130 ~~explaining the spatial interpolation of q_h to create~~ for representing the model's horizontal spatial variability of W_h trough spatial interpolation creating a fog harvesting potential map.

2.1 Thermodynamic module: obtaining liquid water ~~content~~ mixing ratio (~~q_t~~ r_l)

Liquid water ~~content~~ mixing ratio is a complex variable to estimate and measure. It can be obtained from complex and computationally expensive atmospheric models (Large-Eddy Simulation (LES); Weather Research and Forecasting (WRF))

135 (Bergot, 2016) or by sophisticated and expensive instrumentation (fog ~~monitors~~ measurements divices; microwave radiometers) ~~(Kim et al., 2022)~~ (Kim et al., 2022; Gultepe and Milbrandt, 2007). However, our objective here is to estimate ~~q_t~~ r_l using routine meteorological data. To achieve this, we propose employing the air parcel method (Wetzel, 1990), which calculates
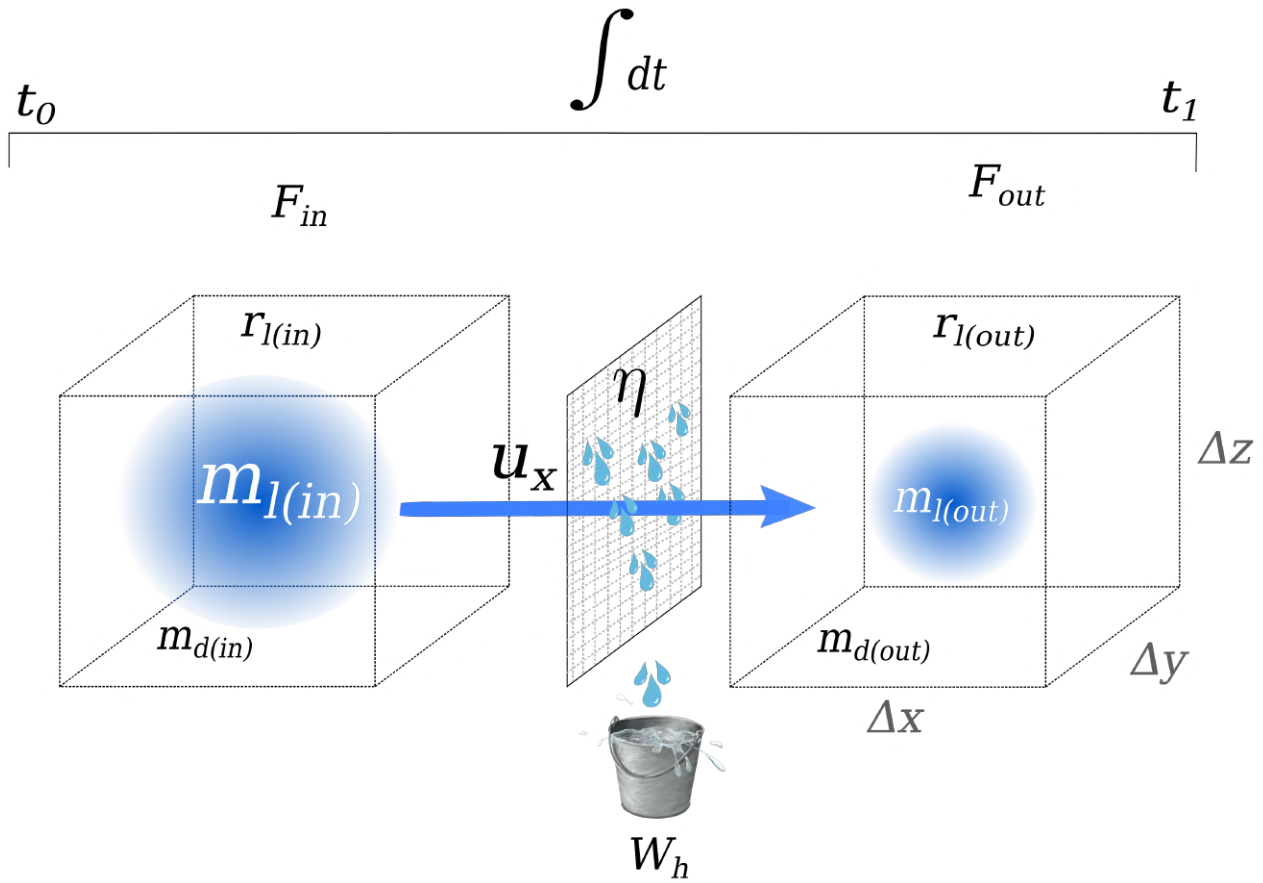
5

Figure 1. ~~Physical~~ AMARU model physical interpretation~~of the~~, including terms from equations (1) ~~and~~ to (27).

thermodynamic changes related to an air parcel while it is uplifted from the surface. The strategy here is to obtain the adiabatic liquid water mixing ratio including the mixing during the lifting. This method has been successfully tested in the Atacama region by Lobos-Roco et al. (2024, 2018), who ~~utilized~~ averaged the meteorological conditions of two meteorological stations located at different heights (z_1 and z_2) along a topographic transect. This strategy allows for observation at ~~two~~ two-combined points within the MBL during advective fog events: z_1 represents near-surface marine meteorological conditions, while z_2 represents inland meteorological conditions close to the MBL top, where fog formation occurs. Figure 2a schematizes the strategy for estimating ~~q_t~~ r_l using the parcel method. This estimation involves four steps, which are described and evaluated in the following subsections.
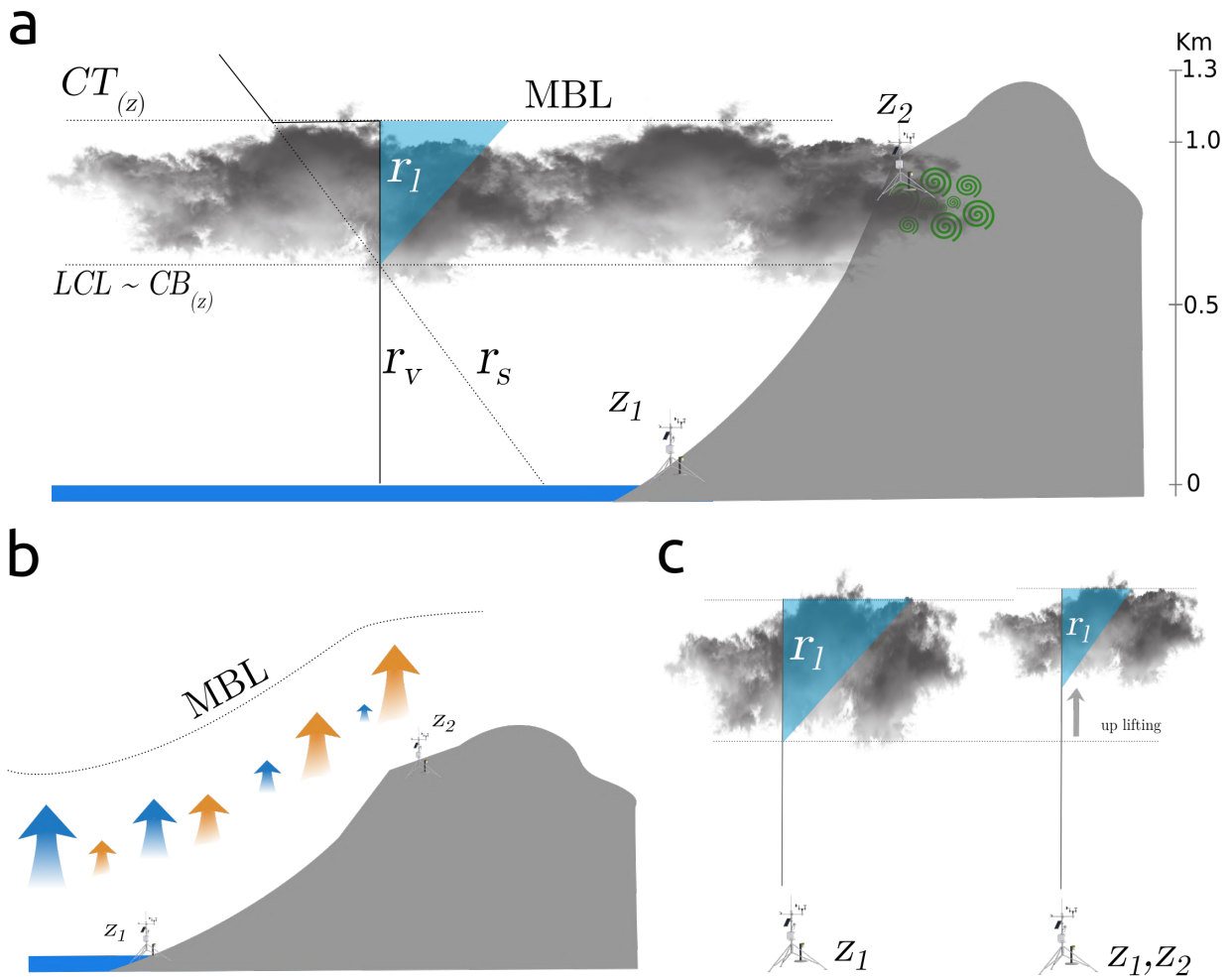
Figure 2. (a) Schematic vertical cross-section representing the estimation of liquid water content ($q_t r_l$) using the air parcel method. (b) Physical representation of the topographic uplifting of Sc cloud and its interaction in the ocean-land transition. Blue (orange) arrows indicate latent heat flux (sensible heat flux) from the surface (c). Representation of the combined meteorological conditions from stations z_1 and z_2 in the cloud base, cloud top, and $q_t r_l$ representation.
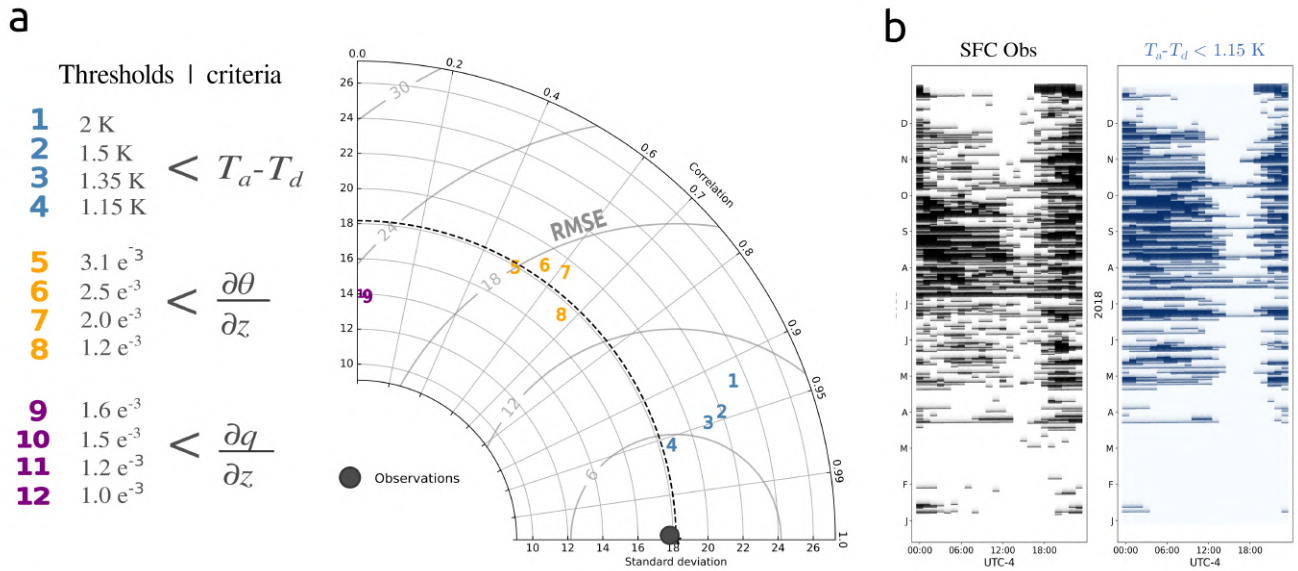
Figure 3. (a) Taylor diagram comparing the proposed criteria and thresholds for estimating fog occurrence. The diagram deploys correlation (r), standard deviation, and root mean square error (RMSE) between the criteria-thresholds and observations. (b) Comparison of the annual diurnal cycle of fog occurrence between observations (SFC) and the best-performing criteria. Note that numbers 11 and 12 have slightly negative correlation, placing behind the line and at the left of y-axis

2.1.1 Fog cover fraction frequency

AMARU is a phenomenological model that relies on the presence of advective fog, which typically occurs under a well-mixed MBL regime (Lobos-Roco et al., 2018). Thus, we propose three criteria for fog estimation using routine meteorological data. The first criterion posits fog occurrence when air temperatures reach the dew temperature (T_a-$T_d = 0$). However, this condition has been rarely observed, particularly in the coastal Atacama, even during fog formation. For this reason, we propose and test four alternative thresholds. For this estimation, we exclusively use data from station z_2. The second criterion is that MBL must be well-mixed. Our criteria for fulfilling this assumption is that the thermal gradient ($\partial\theta/\partial z$) between $\theta_{(z1)}$ and $\theta_{(z2)}$ is minimal. Here, we propose and test four thresholds close to 0 K m^{-1}. The third criterion is similar to the second one but employs the specific humidity vertical gradient ($\partial q/\partial z$) to assess MBL mixing. Similar to the first criterion we propose and test four thresholds to determine how well-mixed is the MBL in terms of temperature and specific humidity.

Figure 3 shows a statistical comparison between the estimated fog occurrence (in %) derived from the three proposed criteria and thresholds, and observations obtained from a Standard Fog Collector, SFC (Schemenauer and Cereceda, 1994). The observations were conducted in the fog oases of Alto Patache (z_2) within the Atacama Desert during the year 2018 (20.82° S; 70.14° W; 850 m ASL, 5 km from the coast). In addition, we also use data from the meteorological station at Diego Aracena Airport, z_1 (20.52° S; 70.15° W; 48 m ASL), to calculate the vertical gradients.

In general terms, among the three proposed criteria, those based on T_a -T_d (blues) show the strongest correlation with directly observed fog collection. Among these, the threshold T_a -$T_d < 1.5$ k (n.4 in Fig. 3a) emerges as the most accurate, exhibiting a standard deviation aligned with observations (18%), a correlation coefficient (r) of 0.95, and a root mean square error (RMSE) of 6%. However, the remaining thresholds yield similar results, suggesting that fog occurs when T_a -T_d spans from 2 to 1.15 K. The second and third criteria are based on the parcel method and the mixing layer theory, which states that Sc cloud formation occurs under well-mixed MBL conditions. The chosen thresholds have been studied before in the coastal Atacama region by Lobos-Roco et al. (2018, 2024), del Río et al. (2021a) and García et al. (2021). The second criteria (depicted in orange) show promising results when compared to observations, displaying a standard deviation ranging between 17 to 20%, an r value ranging from 0.5 to 0.7, and a RMSE of ~17%. These values suggest that the MBL tends to be thermally well-mixed (exhibiting minimal vertical gradients) during fog occurrences. The last criteria (purple ones) demonstrate insufficient performance in detecting fog occurrence, exhibiting no correlation with observations. This suggests that fog occurrence is not contingent upon MBL being well-mixed in terms of moisture. The disparity in the correlation between thermal and moisture vertical gradients with fog frequency can be attributed to the aridity of the observation location. On one hand, the arid terrain thermally contributes less to the MBL during fog events (low radiation during the day over the coastal arid), showing well-mixed MBL. Conversely, when fog is absent, ~~the arid terrain contributes more thermally, leading to a~~ for example during night, the arid slopes contributes to a stable stratified MBL. On the other hand, the arid landscape does not contribute moisture to the MBL during fog occurrences, nor does it when fog is absent, thereby showing no correlation with fog frequency. Figure 3b illustrates the diurnal cycle of fog frequency observed at the Alto Patache fog oasis throughout the year 2018, as measured by the Standard Fog Collector (SFC) and estimated using the threshold with the best performance (number 4). This threshold successfully estimates fog occurrence using simple meteorological data for any day and time throughout the year.

2.1.2 Cloud Base, CB

Once fog occurrence is estimated, we proceed to calculate the height of the fog-cloud base (CB). This process is summarized in Figure 2. The calculation assumes that the lifting condensation level (LCL) in boundary layer clouds such as Sc is equivalent to the cloud base. To compute this, we adopt two approaches inspired by the parcel method of (Wetzel, 1990). The first approach solely considers data from the lowest station (z_1), representative of surface-marine conditions, where LCL corresponds to the height at which ~~q~~ mixing ratio equals to saturated mixing ratio: r_v-~~q_s~~r_s=0, (Fig. 2a). This LCL represents the CB over the ocean.

The second approach considers two physical processes involved in the Sc-to-fog transition: environmental mixing and topographic uplifting. ~~To~~ Firstly, to represent the mixing with the environment experienced by an air parcel during adiabatic ascent, and based on (Lobos-Roco et al., 2018), we combined the meteorological conditions measured at both transect stations (z_1, z_2) using a mixing parameter ~~m~~ m as follows:

9

$$\psi^p_{(z)} = (1 - m\frac{z}{z_{LCL}})\psi^s + (1 - m\frac{z}{z_{LCL}})\psi^{ML}, \tag{8}$$

Where ψ is a scalar for potential temperature (θ) or specific humidity (q), ~~sub-fix~~ super script p represents the state of the air parcel, ~~numbering sub-fix indicates the~~ s indicates the conditions at the lowest station used (z_1), ~~z_2),~~ ML refers to mixed-layer,
which is an average of conditions observed at the two stations, m is the mixing parameter ranging from 0 (no mixing) to 1 (maximum mixing), and z_{LCL} is the ~~LCL calculated using only the z_1 station. Then, the LCL is iteratively calculated using θ_p~~ ~~and q_p, resulting from the combination of stations~~ height at which LCL is reached. Secondly, to account for the inland effect (observed at z_2 station), LCL is calculated iteratively using an averaged θ and q (ψ^{ML}) from z_1 and z_2~~in each iteration. To~~ ~~represent the topographic uplifting, we iterate the LCLcalculation using Equation 3, with the number of iterations representing~~ ~~the degree to which land~~. This ψ^{ML} and LCL are used in Equation 8 to estimate the air parcel state $\psi^p_{(z)}$, which is then used to calculate a new LCL. This calculation is repeated several times, with ψ^{ML} being re-averaged with the conditions at station z_2 in each iteration. This repetitive calculation ensures that the inland conditions (z_2) ~~dominate marine conditions (~~in the MBL's state are accurately represented. Our estimations show that the appropriate number of iterations is related to the distance in km between z_1 ~~) and vice versa when Sc is advected inland~~and z_2. For example, if z_1 and z_2 are separated by 5 km, we iterate five times.

The physical interpretation of this topographic uplifting is depicted in Figure 2b, where the initial iteration represents an equal (averaged) influence of marine (z_1) and inland (z_2) conditions. Subsequent iterations represent the dominance of inland conditions over marine conditions. ~~Our estimations show that the appropriate number of iterations is related to the distance in km between z_1 and z_2.~~Dominant marine conditions exhibit a higher latent heat flux (blue arrow in Fig. 2b) compared to sensible heat flux (orange arrow in Fig. 2b). Conversely, inland-dominant conditions showcase a prevalence of sensible heat fluxes over latent heat fluxes (Fig. 2b). The shift in surface energy partitioning towards dominant sensible heat flux (inland conditions) leads to the LCL being reached at a higher altitude, resulting in the uplifting of the Sc cloud (Fig. 2c). This phenomenon is due to the warmer and drier conditions prevalent over land. It is important to note that during the advection of the Sc cloud, the MBL remains well-mixed, thereby minimizing differences between marine (z_1) and inland conditions (z_2).

To assess the accuracy of our CB estimations, Figure 4 presents a multi-temporal comparison between CB estimations derived from the AMARU model and observations conducted in the Atacama Desert in 2017 as a part of the Ground Optical Fog Observations (GOFOS) experiment (del Río et al., 2021a). The GOFOS experiment entailed year-long monitoring of cloud base and top dynamics during an ENSO-neutral year (2017), employing optical cameras placed across the terrain to record the vertical movement of Sc cloud and fog. The left panel of Figure 4a illustrates that CB estimates generated by the model using Equation ~~3 (CB$_{mod(3)}$~~ 8 (CB$_{mod(8)}$) closely align with those observed in 2017. The mean values of the estimated CB stand at 879 m compared to the observed average of 870 m, with similar standard deviations of 88 m and 93 m, respectively. This satisfactory performance of the model in estimating CB is also observed at a monthly scale in Figure 4b, where the estimated CB generally differs by $\sim$50 m from the observed values on a monthly basis. To assess the model's capacity to replicate the
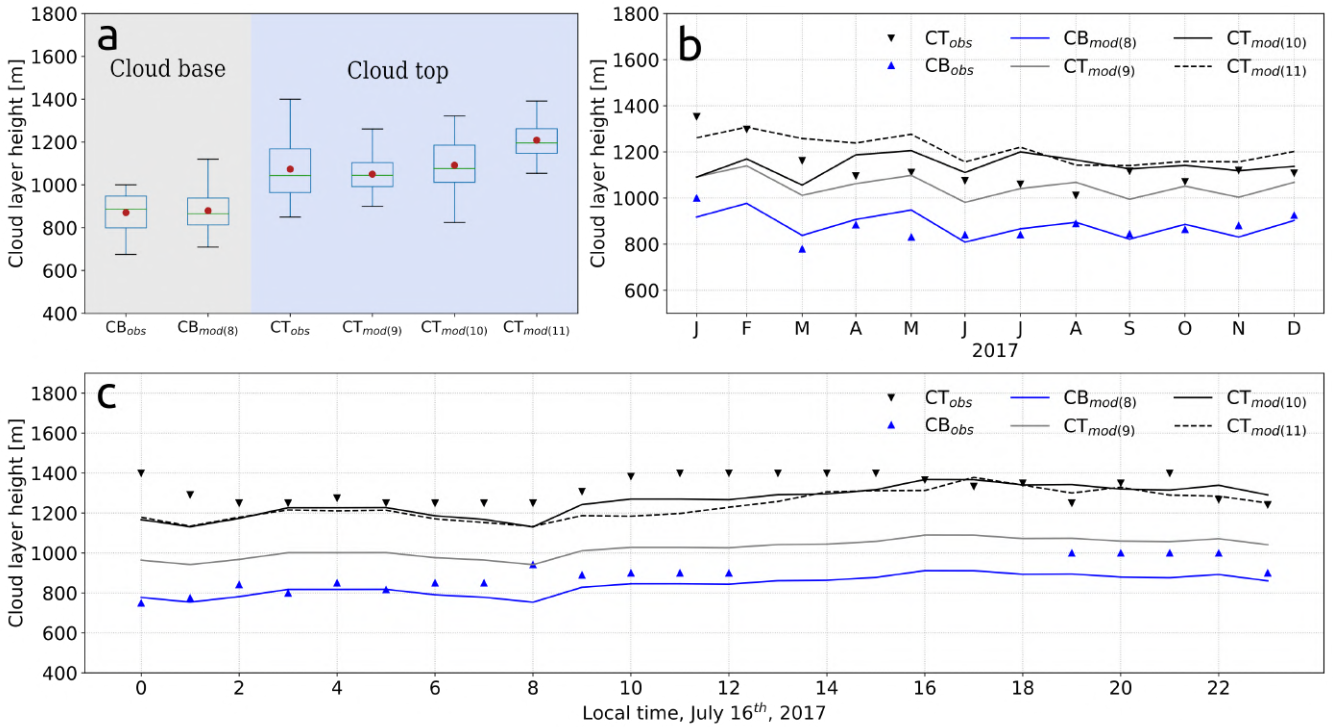
Figure 4. (a) Annual, (b) monthly-averaged, and (c) typical diurnal cycle of CB and CT comparisons between observations (obs) and modeling (mod). The number ~~sub-fix~~ sub scripts refers to the equation number in sections 2.1.2 and 2.1.3.

diurnal cycle of CB, Figure 4c shows a representative foggy day in the Atacama region. It is evident from the figure that the
225 estimated CB closely tracks its diurnal cycle, with errors of ~100 m observed during the afternoon.

2.1.3 Cloud Top, CT

The parcel method, upon which our CB calculations are founded, determines q_t–r_l from the LCL level upward, according
to atmospheric pressure decreases. However, atmospheric pressure also decreases beyond the MBL, where the Sc stands.
Consequently, it becomes necessary to estimate the Cloud Top (CT [m]) in order to calculate the q_t–r_l within the cloud layer.
230 Given the challenges associated with estimating CT using basic meteorological data and taking advantage of the homogeneity
of Sc as a cloud layer, we propose estimating CT as a function of modeled CB using three simple linear regression models.
These models are phenomenological expressions based on CT measurements obtained during the GOFOS experiment in 2017
(del Río et al., 2021a). The proposed linear regression models are as follows:

$$CT_{~~mod(4)~~\underline{mod(9)}} = 236.47 + 0.9355(CB) \tag{9}$$

$$CT_{~~mod(5)~~\underline{mod(10)}} = CB + CB\sqrt{\frac{FCF}{2}} \tag{10}$$

$$CT_{~~mod(6)~~\underline{mod(11)}} = 236.47 + 0.9355(CB)(1 - \frac{\partial\theta}{\partial z})100 \tag{11}$$

Equation ~~4~~ 9 shows a linear regression model in which CT [m] is solely dependent on CB [m]. Equations ~~5 and 6~~ 10 and 11 correspond to linear regression models where CT is determined by CB and fog occurrence. The FCF (fog cover fraction [%], section 2.1.1.) in Equation ~~5~~ 10 and the vertical thermal gradient ($\partial\theta/\partial z$ [K m^{-1}], Fig. 3a) in Equation ~~6~~ 11 are based on observations conducted during the GOFOS experiment, where CT demonstrates a negative correlation with fog frequency (del Río et al., 2021a). A comparable linear regression model, combining CB and fog occurrence to estimate CT, has been tested in various locations within the coastal Atacama region by Lobos-Roco et al. (2024).

Figure 4 shows the effectiveness of linear regression models in predicting CT compared to observations obtained from the GOFOS experiment. The right panel of Figure 4a shows the performance of the three linear regression models against observations for the year 2017. The annual means of the three models are similar to the observed value of (1073 m), with respective values of 1050 m, 1091 m, and 1209 m. However, the CT derived from Equation ~~5~~ 10 is the one that performs better, exhibiting a standard deviation of 142 m compared to the observed value of 124 m. At the monthly scale (Fig. 4b), the CT estimated by Equation ~~6~~ 11 overestimates observations by 150 m. However, the CT from derived from equations ~~4 and 5~~ 9 and 10 remains within a 50 m range of the observed values. In Figure 4c, showing a representative diurnal cycle during the foggy season, both observed and modeled CTs are presented. Here, it is evident that the CT estimated by equations ~~5 and 6~~ 10 and 11 demonstrate a better performance, closely aligning with observations (black triangles). However, the CT estimated from Equation ~~4~~ 9 underestimates observations by over 200 m. These three linear regression models offer a statistical framework for estimating CT, with performance varying based on temporal scale. Henceforth, in this manuscript, we adopt the CT derived from Equation ~~5.~~ 10.

2.1.4 Liquid Water ~~Content~~ Mixing Ratio

Once we have estimated fog occurrence (FCF), the fog Cloud Base (CB), and Cloud Top (CT) using simple meteorological data from a topographic transect, we proceed to determine the adiabatic liquid water ~~content q_l~~ mixing ratio r_l within the cloud layer (z: CT-CB). To achieve this, we utilize the following equation:

$$q_{l(z}r_{l(z)} = q_{(z)}r_{v(z)} - q r_{s(z)}; q r_l \geq 0 \tag{12}$$

where ~~q is the total specific humidity, q_s~~ r_v is the mixing ratio between mass water vapor by kilogram of dry air, r_s denotes the saturated ~~specific humidity, and~~ mixing ratio, and z represents the vertical level between CB and CT (Fig. 2a). It is important to note that, using a combination of z_1 and z_2 stations as in Equation ~~3~~8, the term ~~q is replaced in each iteration by $q_{1,2}$. Regarding q_s, since this term is dependent~~ r_v is assumed as the specific humidity of the mixed MBL (q^{ML}), and r_s depends on absolute temperature, ~~therefore~~ it is influenced by ~~$\theta(1,2)$~~θ^{ML}.

Figures 5a and 5b show the validation of the model-estimated ~~liquid water content (q_l~~ adiabatic liquid water mixing ratio (r_l) against observations of liquid water content (LWC) (CLU, 2024) derived from combined measurements of a microwave radiometer with a Doppler lidar (Schween et al., 2022), conducted at the Diego Aracena Airport in the coastal Atacama Desert during July 2018. ~~Our estimations of liquid water content obtained from Equation (7) systematically double the observed values. Consequently, we applied a correction factor of 0.5 to our estimations, as illustrated in Figure 5b.~~

In general terms, Figures 5a and 5b show a satisfactory comparison between our modeled estimations of liquid water content and the measured ones. The mean observed values peak at 0.1 g m^{-3} at 800 m altitude, while our mean estimations peak at ~~0.08~~ 0.09 g m^{-3} at the same altitude ($\sim$800 m), consistent with typical values found in marine Sc clouds. ~~Likewise,~~ When analyzing the 0.95 percentile curve (red line in Fig. 5) ~~closely tracks~~ the model follows the vertical distribution of observations, exhibiting peaks of ~~0.4~~ 0.7 g m^{-3} between ~~800 m (modeled) and 1000 m(observed)~~ 700 snd 900 m ASL when observation shows peaks of 0.5 g m^{-3}. Upon comparing the ~~maximum hourly-averaged values (grey dots) between the~~ model and observations percentile 0.95, we observe that the model overestimates observations by $\sim$~~0.1~~ 0.2 to 0.3 g m^{-3}. Finally, upon integrating the vertical column of LWC, we ~~observe significant~~ also observe similarities in the mean liquid water path (LWP) with values of ~~1.8 kg~~ 3.6 g m^{-2} and ~~1.6~~ 2.6 kg m^{-2} for modeled and observed data, respectively. To validate the results obtained from the thermodynamic module of the AMARU model, Figure 5c presents the temporal evolution of a simulated fog cloud during a fog event occurring between July 16th and 25th, 2018, at the Alto Patache site. The figure illustrates the model's capability to accurately represent fog-cloud frequency, its vertical structure, and water density (~~q_l~~r_l) over time. In terms of fog frequency, our model shows fog-cloud formation from the 17th to the 19th and from the 22nd to the 24th, aligning with the periods of highest fog collection rates (grey bars). From the 19th to the 22nd, our model does not depict cloud formations, consistent with near-null fog water collection during this period. Likewise, we observe that changes in the vertical structure of the cloud (base and top) correspond to variations in liquid water content and fog collection.

In summary, our straightforward methodology, employing a topographic transect of meteorological stations, effectively estimates the ~~q_l~~ r_l within the MBL vertical column. This estimation is achieved by combining thermodynamic principles and statistical regressions, supported by climatological observations. Notably, our approach not only provides estimates of ~~q_l~~ r_l but also of fog frequency and the vertical structure of the fog cloud, thus enhancing our understanding of the fog phenomenon in coastal arid regions.
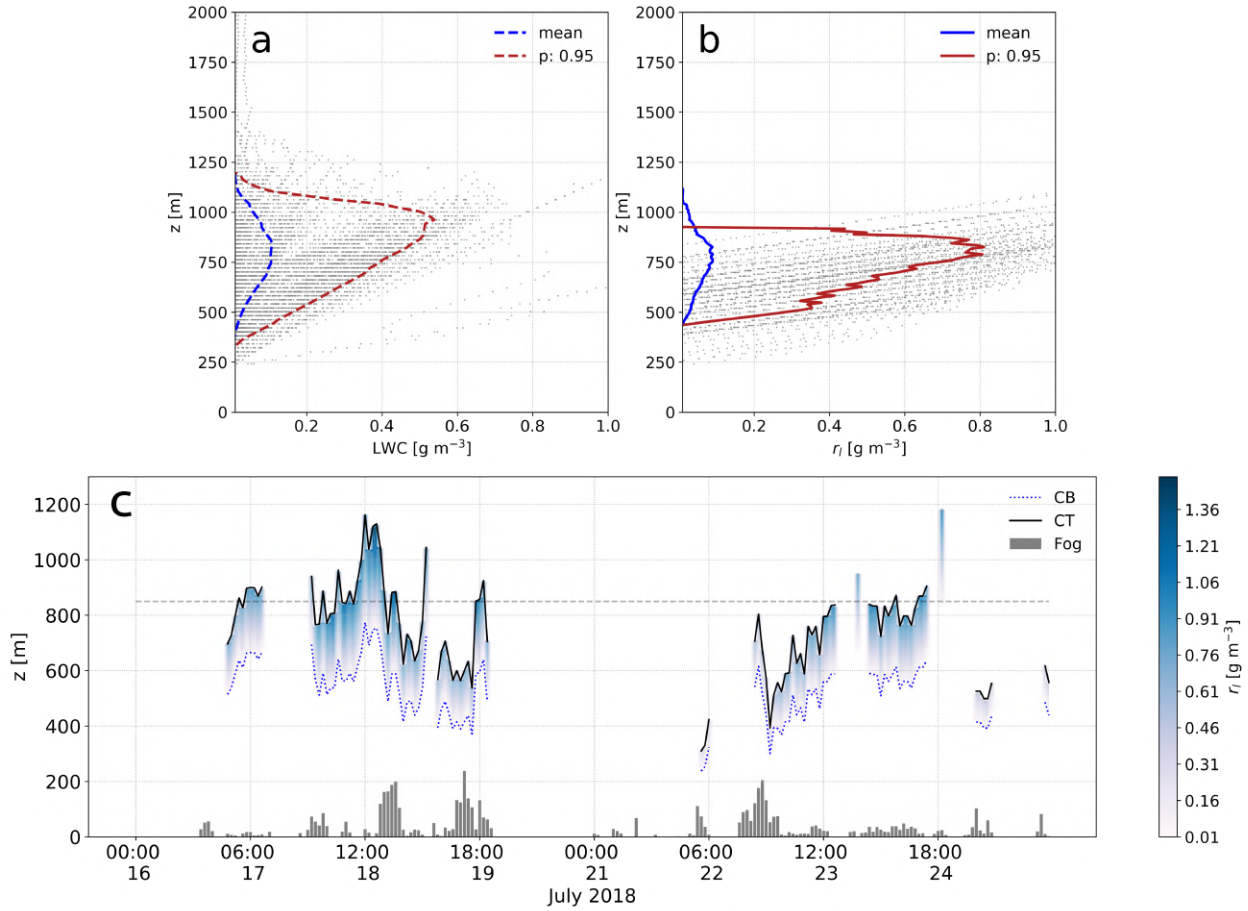
Figure 5. Vertical profiles q_l r_l (in g m^{-3}) (a) derived from a microwave radiometer and Doppler lidar observations (Schween et al., 2022; CLU, 2024) and (b) estimated by the AMARU model over Diego Aracena Airport. Grey dots represent hourly-averaged profiles filtered by percentile 0.99; red lines represent percentile 0.95, and the blue line represents the mean. (c) The evolution of the vertical profile simulated by the AMARU model for the Alto Patache Site. Grey bars at the bottom represent fog collection measurements at 850 m (dashed line).

Coordinate	Altitude	Time period	mean	25%	50%	75%
19.17° S- 70.17° W	850 m	2022	16%	5%	13%	26%
20.48° S- 70.05° W	1200 m	2019	26%	6%	16%	30%
20.82° S- 70.14° W	850 m	2018	~~36~~24%	~~18~~11%	~~34~~19%	~~51~~31%
30.65° S- 71.68° W	630 m	2022	27%	6%	20%	45%
32.16° S- 71.49° W	650 m	2022	15%	4%	5%	21%

Table 1. Descriptive statistics of the empirical efficiency coefficient η estimated in five fog collection stations along a 2000 km coastal strip in Chile.

2.2 Water potential module: ~~Maximum Water Potential (MWP) and~~ collector efficiency coefficient (η)

The second critical parameter in our proposed model is the collector efficiency coefficient (η). This variable is intricately linked with complex processes and factors such as wind flow, liquid water content, droplet size, collector positioning, material properties, mesh curvature and porosity (Carvajal et al., 2020). To ensure our assumptions align with climatological observations, we
determine the collector efficiency using an empirical coefficient. This coefficient~~is defined~~, previously defined in Equation 4, now is redefined as the ratio between the ~~Maximum Water Potential (MWP) and observed fog collection~~observed fog collection (f_{obs}) and the fog inflow (F_{in}), where $f_{obs} = W_h$. As a ratio, η represents the percentage of the maximum water that a fog collector can potentially capture under given atmospheric conditions. η is calculated as follows:

$$\eta = \frac{f_{obs}}{MWP}, \frac{f_{obs}}{F_{in}}. \tag{13}$$

~~where:~~

$$MWP = uq_l A$$

~~and f_{obs} represents the fog collection observations.~~Note that both ~~MWP~~F_{in} and f_{obs} are averaged per hour, therefore both terms have the unit of L m^{-2} h^{-1}. Since η is calculated based on fog observations, its value depends on the type of collector used, providing flexibility to the model to adapt to different collector types if observations are available.

Table 1 shows the empirical collector efficiency coefficient (η) calculated for five fog collection stations located between 600 and 1200 m along the coastal strip of Chile. Overall, η varies from 15% to 36%, with a variability ranging from 4% to 50%. Three factors contribute to this variability in the efficiency coefficient. Firstly, the model's ability to accurately determine fog frequency (RMSE of 6% in Fig. 3a) can lead to discrepancies, potentially resulting in very high ($\eta \sim 100\%$) or null (~~ηequation~~ ~~$\sim \eta$~~$\sim 0\%$) efficiencies when fog collection is observed, thus altering the averages. Secondly, wind speed may also play a significant role, as it is responsible for transporting ~~q_l~~r_l through the collector. Lastly, both the material of the mesh and its

curvature during fog collection could impact mesh efficiency (Carvajal et al., 2020). Despite the variability in η across all sites, we find an average efficiency coefficient of ~~22~~25% $\pm$ 10%, consistent with results in the literature. For instance, Montecinos et al. (2018) reported efficiencies ranging from 0% to 36% in large fog collectors. Similarly, using numerical simulations, Carvajal et al. (2020) reported a mean efficiency of 28% with a theoretical maximum of 36%. Finally, de Dios Rivera (2011) reported maximum fog collection efficiencies between 20% and 24% using a simple numerical model approach for different mesh types.

For our study, we use an η between 0.25 (25%). Once η is estimated, we can readily solve Equation (~~2~~6) to obtain an estimation of fog water harvesting (~~q_h~~W_h). Given that ~~q_l~~r_l has a vertical dimension, assuming a constant wind speed (u) along the MBL, we can derive the vertical distribution of fog harvesting.

2.3 Spatial module: fog harvesting maps

In addition to the thermodynamic module, we propose a spatial module for ~~interpolating~~ extrapolating the vertical variability of ~~q_h~~W_h into a horizontal spatial domain. To do it, we integrate the ~~thermodynamic and water potential modules results with two satellite products:~~ vertical domain (z) of W_h to an area of optimal fog harvesting potential obtained from a combination of a digital elevation model (DEM) and GOES satellite images. We outline four steps to achieve this spatial variability.

The first step involves reclassifying the DEM ~~pixels~~ grid cells based on the cloud layer height ~~, removing all pixels~~ and removing all grid cells below the CB and above the CT elevation. This reclassification ensures that only the ~~altitude~~ elevation range where the Sc cloud could potentially impact the topography is considered. In the second step, we create an aspect image (slope orientation) with the DEM and reclassify the pixels based on the ~~range angle~~ angle range of the main wind direction (mean $\pm$ std) when fog is collected (obtained from observations at the z_2 station). The third step involves calculating the fog and low cloud (FLC) frequency using data from the GOES satellite ~~(del Río et al., 2021b; Lobos-Roco et al., 2024)~~ (del Río et al., 2021b; Espinoza et al., 2024). This algorithm continuously calculates the presence and absence of FCL in every ~~pixel~~GOES grid cell. The third step serves as a ~~spatial~~ geographical framework, delineating the area where fog-cloud ~~interaction with topographyoccurs~~interacts with topography. The spatial intersection of the three steps generates optimal areas for fog collection, physically representing the locations where the Sc cloud ~~intersects with~~ and its harvesting potential intersect the surface. It is important to note that the values of ~~pixels~~ grid cells in these optimal areas for fog collection represent ~~altitudes~~ elevations (m ASL) in areas with high FLC frequency. The final step involves replacing the ~~altitude pixel~~elevation grid cell values of the optimal fog collection areas with the vertical distribution of potential fog harvesting (~~q_h~~W_h). As ~~q_h~~W_h values are associated with a vertical domain (z), each ~~q_h~~Wh value can be mapped onto the resulting grid of optimal fog collection areas. The result of this last step yields a spatial distribution of potential fog harvesting.

3   Model applications to (semi-)arid study case sites

The AMARU enables us to evaluate the spatiotemporal variability of fog harvesting using routine meteorological data and satellite products. In this section, we evaluate the application of the model (~~q_n~~W_h) at three sites along the coastal strip of Chile corresponding to hyper-arid, arid, and semi-arid ecosystems between 2018 and 2023.

Figure 6 shows the geographical setting of the study sites, which correspond to hyperarid (Site a), arid (Site b), and semi-arid (Site c) fog ecosystems situated between 600 and 1200 m ASL along the coastal mountains of Chile. Generally, these sites represent xeric ecosystems (Muñoz-Schick et al., 2001) sustained year-round by fog, with a frequency exceeding 40% (Fig. 6). Each of these three sites is equipped with meteorological and fog collection observations, managed by the Centro UC Desierto de Atacama of Pontificia Universidad Católica de Chile. The characteristics of these stations and their data and parameters used in the model are summarized in Table 2. In addition, to meet the model's requirements, observations from these three sites (z_2) are complemented with data from near-sea level observations (z_1), sourced from public datasets (www.agromet.cl), which are also detailed in Table 2.

Site	Coordinates	Height	Distance coast	η	Available data	Time period
a_{z_2}	20.82° S-70.14° W	850 m	5 km	~~36~~25%	T, RH, P, U, WD, fog collection	01-01-2018
a_{z_1}	20.52° S-70.15° W	48 m	1 km		T, RH, P, U, WD	31-12-2018
b_{z_2}	26.00° S-70.60° W	820 m	2 km	~~22~~25%	T, RH, P, U, WD, fog collection	01-05-2023
b_{z_1}	26.29° S-70.62° W	120 m	2 km		T, RH, P, U, WD	~~31-12-2023~~31-10-2023
c_{z_2}	32.16° S-71.49° W	650 m	3 km	~~22~~25%	T, RH, P, U, WD, fog collection	~~01-01-2022~~01-09-2022
c_{z_1}	32.16° S-71.51° W	60 m	1 km		T, RH, P, U, WD	31-12-2022

Table 2. Geographic characteristics and available data of observational sites (z_2) and their corresponding stations at the coast (z_1). T represents air temperature at 2 m, RH relative humidity, P air pressure, U wind speed, and WD wind direction.

3.1   Seasonal cycle of modeled and observed fog harvesting

AMARU satisfactorily reproduces the observations of fog harvesting in both magnitude and variability over time. Figure 7 shows a comparison of monthly-average daily rates of fog harvesting at the three analyzed sites. Overall, the model results (blue) follow the seasonal cycle of observed fog collection (grey) across latitudes, albeit ~~underestimating observations by 2~~showing disagreements with observations by 1% to 20%. In the hyperarid environment of Site (a) (Fig. 7a), the model estimates an annual daily rate of ~~4.1~~5.0 L m^{-2} d^{-1}, which satisfactorily compares to the rate of 5.5 L m^{-2} d^{-1} obtained through observations. Likewise, the model can closely track the seasonal cycle of fog harvesting, exhibiting low rates in summer (JFM) and autumn (AMJ) and higher rates in winter (JAS) and spring (OND). Moreover, the model correctly estimates the frequency of fog events. For instance, during summer, the model estimates a very low (JM) or null (F) fog collection, with errors around 0.39 L m^{-2} d^{-1} (20%) compared to observations. Similarly, during the optimal fog harvesting season between winter and spring, the model correctly estimates the monthly magnitude of observed fog collection with errors of 2 L m^{-2} d^{-1} (18%).
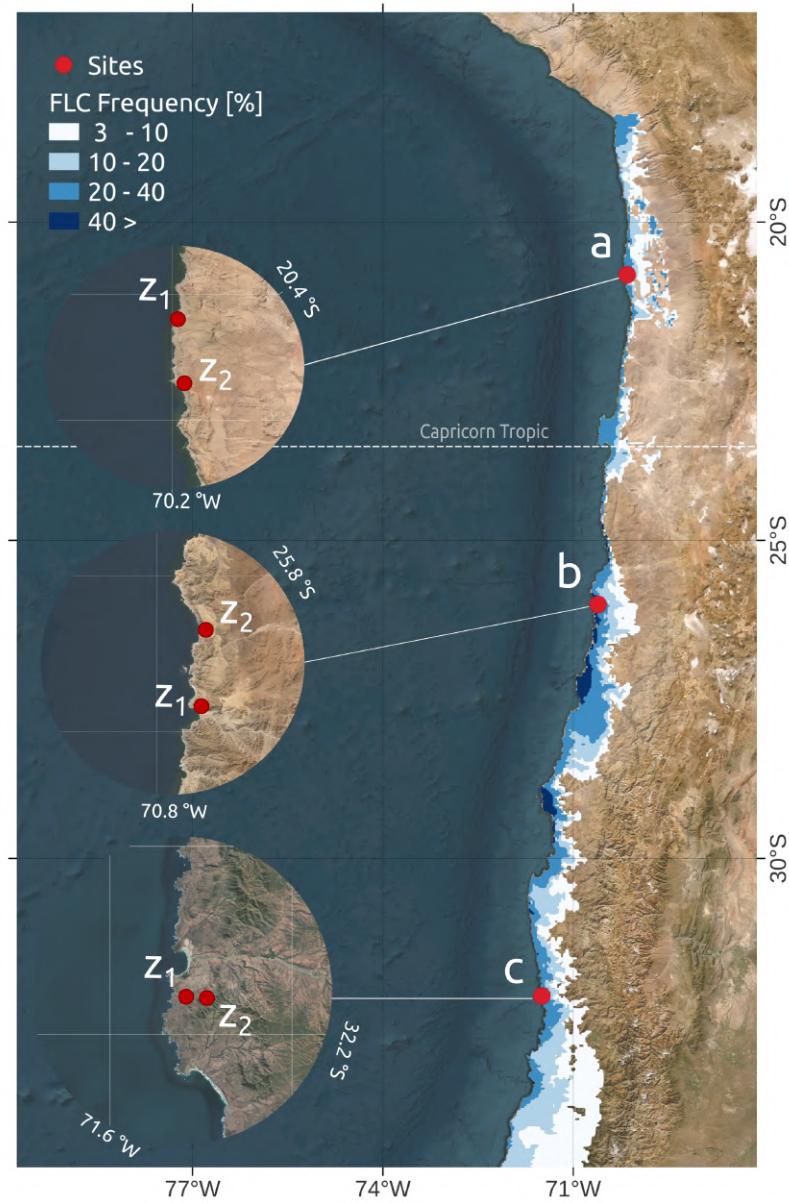
Figure 6. Location of the study sites and their meteorological stations. The blue-coloured areas represent the fog and low cloud (FLC) frequency obtained by the GOES satellite (del Río et al., 2021b) between 2018 and 2023. z_1 and z_2 represent the meteorological stations forming the transect used for running the model according to our methodology.

Finally, the model successfully replicates the variability in the monthly daily rates of fog collection as indicated by the error bars. In spring, for example, the observed rates range from 4 to 9 L m^{-2} d^{-1}, while the model estimates rates range from 6 to

365   10 L m^{-2} d^{-1}.

For Site (b), situated in an arid environment (Fig. 6), the amount of fog collection is notably lower compared to Site (a) (hyperarid). However, the model accurately reproduces the annual-averaged daily rate of fog harvesting ~~with a slight underestimation of 2.6%~~ of 4.3 L m^{-2} d^{-1}. Despite this overall good performance, the model still underestimates observations by approximately ~~50~~20% during winter-spring in terms of magnitude and variability (as indicated by the error bars).

370   Unfortunately, the annual cycle for Site (b) remains incomplete as observations began only ~~in May~~ from May to October 2023. For the semi-arid environment of Site (c) the model shows annual daily rates of fog harvesting similar to those of Site (b), albeit with an overestimation of ~~5.8~~20% compared to observations. During ~~months with the lowest fog collection rates (March to July), the overestimation amounts to 1.8 L m^{-2} d^{-1}. Conversely, during~~ the months with the highest fog collection rates (~~August~~ September to December), the model ~~underestimates~~ overestimates observations by ∼~~2~~1 L m^{-2} d^{-1}. It is worth men-

375   tioning that these discrepancies in estimation are not systematic, and despite them, the model captures the same seasonal cycle obtained through observations at all three sites.

3.2 Vertical variability of fog harvesting potential (~~q_h~~W_h)

Since the model estimates the liquid water content (~~q_t~~r_l) in the vertical column of the Sc cloud when it interacts with topography, and assuming constant wind at z_2 throughout the vertical, we can model the fog harvesting potential at every height within

380   the Sc cloud layer.

Figure 8 shows the vertical variability of ~~q_h~~W_h potential for the three analyzed sites. In the figure, dots represent the total ~~q_h~~W_h per hour at each height within the fog-cloud layer over the course of one year. The red line depicts the annual average daily rate of ~~q_h~~W_h as a function of height, while the black dot shows the observed annual average daily rate. In addition, the dots are colour-coded based on the corresponding ~~q_t~~r_l values. From Figure 8, it is evident that fog harvesting potential decreases

385   from the hyperarid (north) to the semi-arid (south) regions for both ~~q_h and q_t~~W_h and r_l. Specifically, in the hyperarid site, a ~~q_h~~W_h of 10 L m^{-2} d^{-1} can be easily reached, whereas in the arid and semi-arid sites, maximum ~~q_h~~W_h of 5 and 3 L m^{-2} d^{-1}, respectively, are observed. The same behaviour is observed for ~~q_t~~r_l, which exhibits higher values (mean percentile 0.95 up to ~~0.44~~0.7 g kg^{-1}) in the hyperarid site compared to the arid and semi-arid sites, where ~~percentile 0.95~~ 0.95 percentile reaches up to ~~0.40~~0.6 g kg^{-1} and ~~0.33~~0.4 g kg^{-1}, respectively. The vertical variability of ~~q_h~~W_h also allows us to study the vertical liquid

390   water capacity of the fog cloud. For instance, in the hyperarid site, the model estimates fog harvesting potential from 600 m up to 1350, while in the arid and semi-arid sites, fog can be harvested from 500 to 1250 and from 370 to 1050, respectively. These variations in ~~q_t~~r_l and the fog cloud layer height are explained in Equation (3) and Figures 2b and 2c. In Equation (3), we show that the calculation of cloud base, and consequently ~~q_t~~r_l, is influenced by the combined conditions of stations z_1 and z_2. For example, in the hyperarid site situated within the tropics (Fig. 6), air temperature is higher at both z_1 and z_2 compared to the

395   semi-arid site. This implies that the condensation of the air parcel in Site (a) will occur at a higher altitude than in Site (b). Likewise, higher temperatures increase the air's capacity to hold humidity, resulting in a higher ~~q_t~~r_l observed in the hyperarid
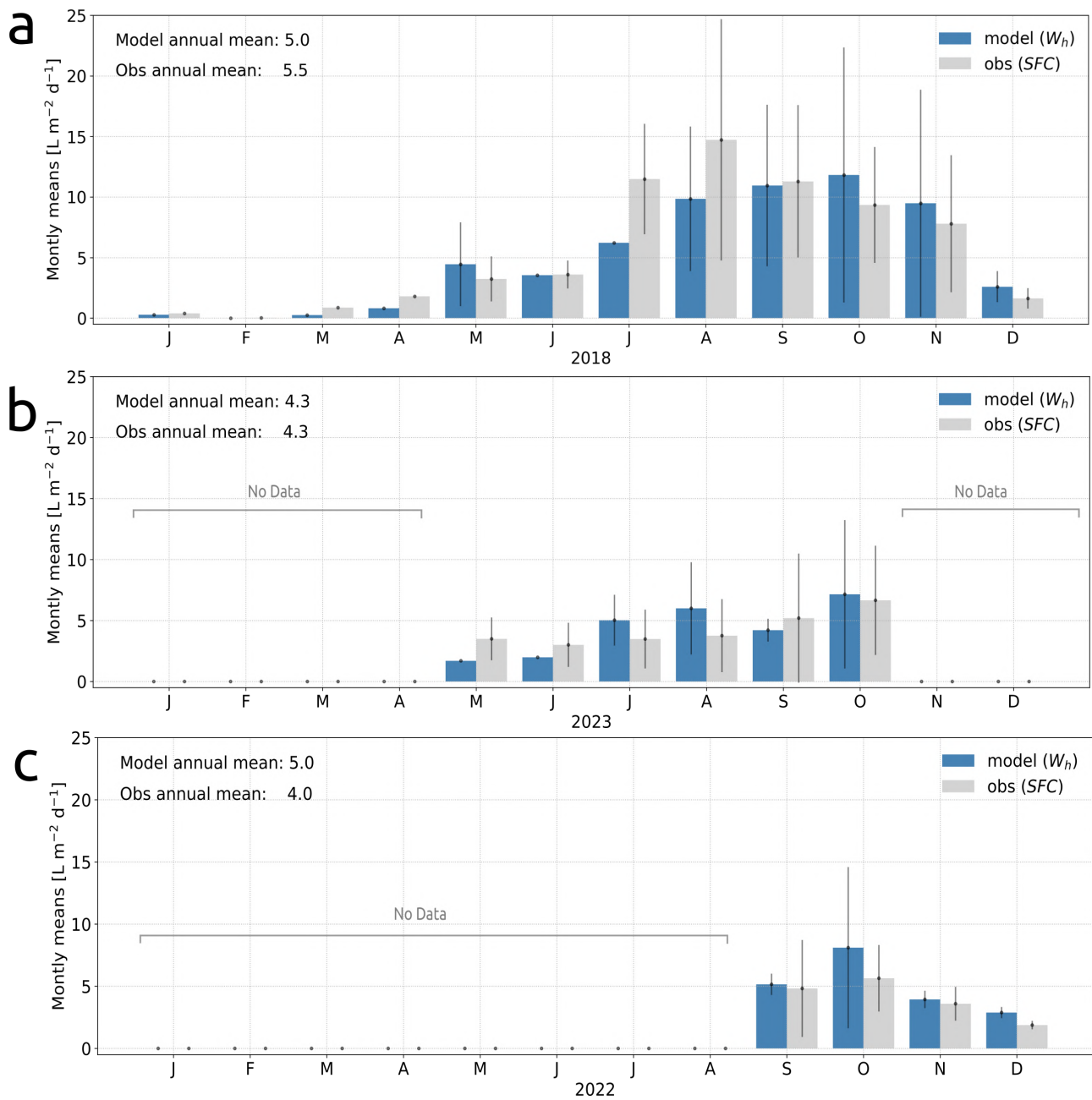
19

Figure 7. Comparison of monthly-averaged daily fog collection rates between model (blue) and observations (grey) in three fog ecosystems situated in the (a) hyperarid, (b) arid, and (c) semi-arid Chilean coast. The error bars show data variability between the 25th and 75th percentiles.

site compared to the semi-arid one. Another significant factor contributing to the difference in ~~q_t-r_l~~ and cloud layer height is the distance from the coast at which station z_2 is located. For instance, the hyperarid site is 5 km inland compared to the arid and semi-arid sites located 2 km and 3 km away from the coast, respectively (Table 2). Consequently, inland conditions in the hyperarid site are hotter than in the other two sites, contributing to the formation of the cloud layer at higher altitudes.

Figure 8 also shows the annual average daily rates (red line) estimated by the model and observed by a standard fog collector (black dot). This red line indicates the vertical placement of the maximum annual ~~q_h~~ W_h. For example, in the hyperarid site, the maximum ~~q_h~~ W_h is located at 900 m in height, while observations are situated at 850 m ASL, explaining the highest annual daily fog collection rates. In contrast, in the arid and semi-arid sites, the maximum ~~q_h~~ W_h is not aligned with the height of the observations. For Site (b) case, the maximum ~~q_h~~ W_h is reached at ∼680 m, whereas observations are located at 820 m ASL. Similarly, for Site (c), the maximum ~~q_h~~ W_h is situated at 500 m, while observations are at 650 m ALS. The validation of annual average daily rates in Figure 8 is determined by the proximity of the black dot to the red line at the observed height. For example, in Figure 8a, we observe an underestimation by the model, which is also evident in Fig 7a, but not in the vertical dimension, as the observations differ by ∼~~1.5~~ 0.5 L m^{-2} d^{-1} from the modeling results. For sites (b) and (c) (Figs. 8b and 8c), the model accurately reproduces the annual daily rates, consistent with the observation, as also observed in Figures 7b and 7c.

3.3 Spatial variability of ~~q_h~~ W_h: fog harvesting potential mapping

The combination of AMARU's results with satellite products enables us to interpolate the influence of the Sc cloud over land and its potential harvesting in space. This subsection introduces two examples of AMARU's results in spatial variability that can be utilized for fog ecosystem delimitation and water planning.

Figure 9a shows the optimal fog harvesting areas highlighted in red, corresponding to the region where the Sc cloud interacts with the Earth's surface. For Site (c), these areas are displayed near the summit of the coastal mountains, specifically ranging from 370 m to 1050 m ASL (Fig. 8c). In addition, based on data from the meteorological Station (z_2) at this site, the fog cloud flux originates from the South and Southeast (110° to 300°), which is reflected in the model's depiction of the mountain slopes facing South and Southeast. In the zoom-out view of Figure 9a, we observe that the extent of these optimal fog harvesting areas spans within the first ∼20 km from the coast, as determined by the frequency of fog and low clouds derived from the GOES satellite (section 2.3).

To independently validate the spatial interpolation of AMARU's results, we compare the optimal fog harvesting areas with fog-dependant vegetation. In Figure 9a, areas highlighted in green represent the normalized difference vegetation index (NDVI) estimated through Sentinel satellite imagery. Overall, the optimal fog harvesting areas align with areas exhibiting the highest NDVI values. For example, a concentration of NDVI is observed at the summit of the mountains and the southeast slopes, indicative of a forest ecosystem sustained by fog (Garreaud et al., 2008). Furthermore, NDVI also concentrates at the bottom of small valleys downstream of the summits, suggesting that fog water accumulated on the summits may potentially flow down, supplementing the precipitation input to the streams.

Figure 9b shows the spatial variability modeled resulting from the intersection between the vertical profile annual average daily rate (red line, Fig. 8a) and the optimal fog harvesting areas. In the figure, we observe the spatial distribution of the fog
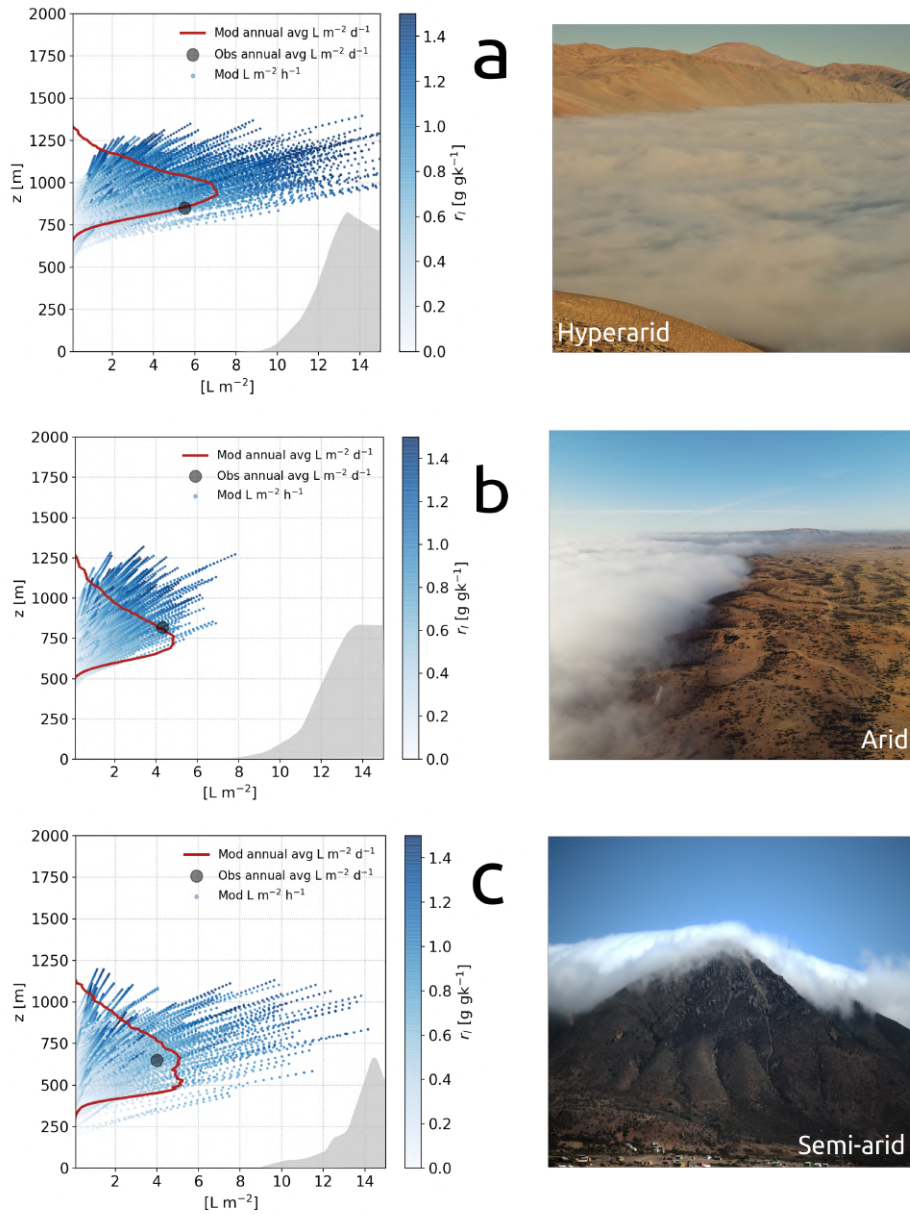
Figure 8. Vertical variability of modeled fog harvesting ($q_h W_h$) in the (a) hyperarid, (b) arid, and (c) semi-arid sites. Dispersed dots represent the total fog harvesting at every hour; the red line is the annual average daily rate of $q_h W_h$, and the grey dot is the observed annual averaged daily rate of $q_h W_h$. The dispersed dots are color-coded in a blue scale representing the liquid water content ($q_t r_l$). The grey shading represents the topographic profile of each site. The right panels show a photograph of each site during a fog event.
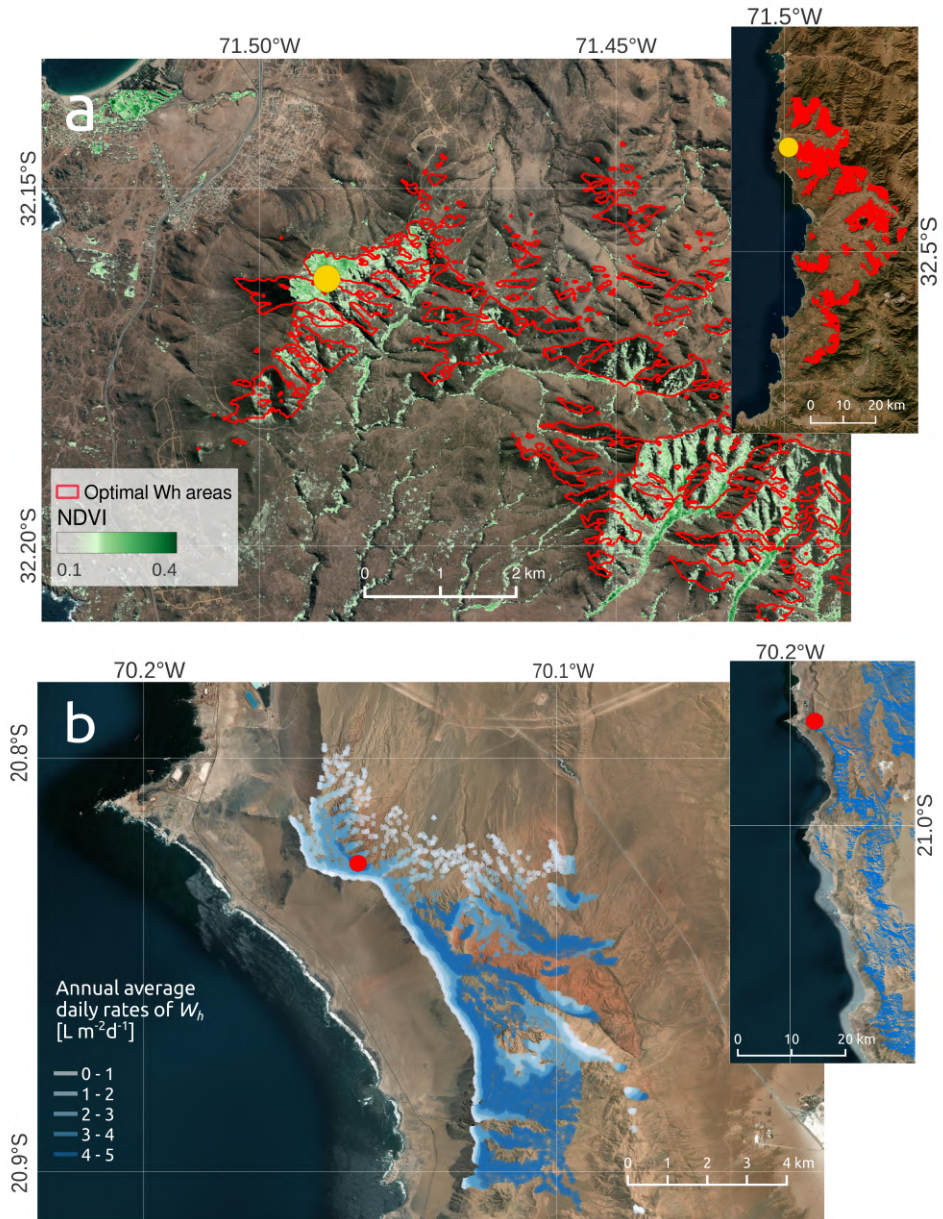
Figure 9. (a) optimal fog harvesting areas (red line) resulting from the model for Site (c) compared to the normalized difference vegetation index (NDVI, ranging from 0.1 to 0.4) estimated through Sentinel satellite images for 2022. The yellow dot indicates the meteorological station (z_2). (b) Spatial variability of annual averages daily rates of ~~q_h~~ W_h for the Site (a) estimated during 2018. The red dot indicates the meteorological station (z_2).

water potential along the mountain, with maximum values observed around 900 m. The topography of the mountain favours altitudes around 900 m ASL with Southwest slope orientations, leading the model to project large areas with fog harvesting potential ranging from 4 to 5 L m^{-2} d^{-1}. In the eastern areas of the meteorological station (red dot, z_2), fog harvesting potential decreases to lower altitudes, consistent with results presented in Figure 8a. Likewise, decreases towards the southwest of the
435 station at higher altitudes until it disappears. The area surrounding the station corresponds to the well-known fog oases of Alto Patache (Muñoz-Schick et al., 2001), situated between 600 and 850 m, within the optimal areas of fog harvesting determined by the model.

This model application is further extrapolated to the entire region to determine optimal fog harvesting spots within the area of influence of fog and low clouds, as determined through the GOES satellite. An example of these larger areas is shown in the
440 zoom-out view of Figure 9b, where optimal fog harvesting areas are situated within 10 km from the coast. Since the model runs with simple meteorological time series, fog harvesting potential maps can be generated for different time averages, enabling us to study and assess the spatial changes in fog harvesting potential over hours (events), days, seasons, and years.

4 Model limitations and challenges

Despite the versatility of the AMARU model in representing the harvesting of the advective fog phenomenon in both time and
445 space, it has several limitations that are worth describing.

Firstly, one of the most important variables in the model is the adiabatic liquid water mixing ratio (r_l), which is estimated assuming water vapor is condensed because it reaches saturation. Despite our simplistic approach and reliable results, we know that further model improvements must be made by including essential microphysical processes. Such processes are mean volume diameter, effective size, droplet concentration, and effective droplet size (Gultepe et al., 2021). To account for
450 these processes, comprehensive observations must be performed to get a complete budget equation allowing us to have more realistic modeling.

Secondly, the model's capability to represent fog harvesting in time is primarily limited by the empirical collector coefficient. However, this coefficient remains constant in the model, resulting in both underestimations and overestimations compared to observations. To improve our estimations of fog harvesting over time, further exploration into the collector efficiency is
455 necessary, incorporating factors such as wind speed, collector material properties, and cloud droplet size into more complex functions.

~~Secondly~~Thirdly, the model's capability to assess fog harvesting potential in the vertical column of the MBL enables us to evaluate the maximum fog harvesting potential beyond single-point observations. However, this vertical ~~q_h~~ W_h estimation is contingent upon accurately determining ~~q_t~~ r_l assuming that wind speed remains consistent at every level of the MBL. Although
460 ~~q_t~~ r_l estimations align with observations from microwave radiometers, our results must be validated with in-situ observations of liquid water content during fog collection. In addition, relevant physical processes influencing CT, such as dry air entrainment from the free troposphere, ~~among other~~ and thermal inversion are not included in its calculation. Instead, CT is statistically estimated, leading to uncertainties in a variable whose precision is crucial for estimating the maximum ~~q_t~~ r_l and, consequently,

~~q_h~~W_h. Regarding wind speed, our assumption of a constant horizontal wind along the MBL is based on the mixed layer theory, which posits that scalars such as potential temperature, ~~specific humidity~~mixing ratio, and wind speed remain constant if the MBL is well-mixed. However, this theory does not consider topography, which may disturb this constant pattern when interacting with MBL winds. To improve the model's estimation of ~~q_l and better q_h~~r_l and better W_h potential, future research must incorporate accurate vertical profile observations of temperature, ~~humidity~~mixing ratio, and wind speed.

Finally, the spatial ~~interpolation of q_h~~extrapolation of W_h represents a preliminary approach for fog harvesting potential mapping. This is because its accuracy is limited by the availability of spatially distributed meteorological data. We spatially ~~interpolate~~ extrapolate the conditions determined by the model for the z_2 station to all surrounding areas that share the same geographic conditions. Nevertheless, this approach may overestimate several inland locations that meet the geographical characteristics of z_2 but not the atmospheric ones. Improving this spatial ~~interpolation of q_h~~extrapolation of W_h can be addressed using two approaches. The first one involves utilizing gridded meteorological data that allows us to solve Equation (26) at every grid point. Unfortunately, available gridded data is often too coarse to accurately represent the sub-kilometer fog harvesting phenomenon. The second approach entails incorporating the FLC frequency determined by the GOES satellite (Fig. 6) into the spatial interpolation of ~~q_h~~W_h. For example, we can modify ~~q_h~~W_h spatially using a function based on the FLC frequency, where locations with similar geographical conditions to z_2 ~~Station~~ station may see their ~~q_h~~W_h reduced (increased) if their FLC frequency is higher (lower) than that observed at z_2 ~~Station~~station.

5 Conclusions

We propose, formulate, and evaluate an observational-driven model, named AMARU, for estimating advective fog ~~liquid water capacity and~~ water potential harvesting in (semi-)arid regions. This model uses standard and routine meteorological observations ~~, enabling us to know~~ to estimate where, when, and how much water can be potentially harvested from fog clouds.

The proposed model employs a thermodynamic approach to estimate ~~the liquid water content of fog~~fog's adiabatic liquid water mixing ratio, incorporating key physical processes associated with the interaction between the stratocumulus cloud and topography. This approach yields vertical profiles of liquid water ~~content~~mixing ratio, from which fog frequency, cloud base, and top can be derived. In addition, by integrating the estimations of liquid water ~~content~~ mixing ratio with climatological records of fog harvesting observations, we derive an empirical collector efficiency coefficient to estimate vertical profiles of potential fog harvesting. Finally, combining vertical profiles of fog harvesting potential with satellite products, we introduce a methodology for spatially ~~interpolating~~ extrapolating these results, thereby generating fog harvesting potential maps.

~~We apply the model to study the~~ Below, we outline the main conclusions of our research.

- Despite the simple approach, this model correctly reproduces essential physical components involved in fog harvesting. Our evaluation with available observations show that model results reproduce: fog frequency (R: 0.95; RMSE: 6%), cloud base and top height (errors <50 m), liquid water content (errors ~0.2 g m^{-3}), and fog collector efficiency

Finally, we expect this research to yield significant social benefits by providing decision-makers with valuable insights into new water sources, thus aiding in the mitigation of climate change impacts.

6

550

28

References

Andersen, H., Cermak, J., Fuchs, J., Knippertz, P., Gaetani, M., Quinting, J., Sippel, S., and Vogt, R.: Synoptic-scale controls of fog and low-cloud variability in the Namib Desert, Atmospheric Chemistry and Physics, 20, 3415–3438, 2020.

Baguskas, S. A., Oliphant, A. J., Clemesha, R. E., and Loik, M. E.: Water and light-use efficiency are enhanced under summer coastal fog in a California agricultural system, Journal of Geophysical Research: Biogeosciences, 126, e2020JG006 193, 2021.

Berbel, J. and Esteban, E.: Droughts as a catalyst for water policy change. Analysis of Spain, Australia (MDB), and California, Global Environmental Change, 58, 101 969, 2019.

Bergot, T.: Large-eddy simulation study of the dissipation of radiation fog, Quarterly Journal of the Royal Meteorological Society, 142, 1029–1040, 2016.

Carvajal, D., Silva-Llanca, L., Larraguibel, D., and González, B.: On the aerodynamic fog collection efficiency of fog water collectors via three-dimensional numerical simulations, Atmospheric Research, 245, 105 123, 2020.

Cereceda, P., Osses, P., Larrain, H., Farıas, M., Lagos, M., Pinto, R., and Schemenauer, R.: Advective, orographic and radiation fog in the Tarapacá region, Chile, Atmospheric Research, 64, 261–271, 2002.

Cereceda, P., Larrain, H., Osses, P., Farias, M., and Egaña, I.: The spatial and temporal variability of fog and its relation to fog oases in the Atacama Desert, Chile, Atmospheric Research, 87, 312–323, 2008.

CLU: Custom collection of liquid water content data from Iquique between 9 and 31 Jul 2018, Tech. rep., Cloud remote sensing data centre unit (CLU)., [Online; accessed 2024-01-05], 2024.

de Dios Rivera, J.: Aerodynamic collection efficiency of fog water collectors, Atmospheric Research, 102, 335–342, 2011.

del Río, C., Lobos-Roco, F., Siegmund, A., Tejos, C., Osses, P., Huaman, Z., Meneses, J. P., and García, J.-L.: GOFOS, ground optical fog observation system for monitoring the vertical stratocumulus-fog cloud distribution in the coast of the Atacama Desert, Chile, Journal of Hydrology, 597, 126 190, 2021a.

del Río, C., Lobos-Roco, F., Siegmund, A., Tejos, C., Osses, P., Huaman, Z., Meneses, J. P., and García, J.-L.: GOFOS, ground optical fog observation system for monitoring the vertical stratocumulus-fog cloud distribution in the coast of the Atacama Desert, Chile, Journal of Hydrology, 597, 126 190, 2021b.

Espinoza, V., Lobos-Roco, F., and del Río, C.: Synoptic control of the spatiotemporal variability of fog and low clouds under ENSO phenomena along the Chilean coast (17°-36° S), Atmospheric Research, p. 107533, 2024.

Estrela, M. J., Valiente, J. A., Corell, D., Fuentes, D., and Valdecantos, A.: Prospective use of collected fog water in the restoration of degraded burned areas under dry Mediterranean conditions, Agricultural and forest meteorology, 149, 1896–1906, 2009.

García, J.-L., Lobos-Roco, F., Schween, J. H., del Río, C., Osses, P., Vives, R., Pezoa, M., Siegmund, A., Latorre, C., Alfaro, F., et al.: Climate and coastal low-cloud dynamic in the hyperarid Atacama fog Desert and the geographic distribution of Tillandsia landbeckii (Bromeliaceae) dune ecosystems, Plant Systematics and Evolution, 307, 1–22, 2021.

Garreaud, R., Barichivich, J., Christie, D. A., and Maldonado, A.: Interannual variability of the coastal fog at Fray Jorge relict forests in semiarid Chile, Journal of Geophysical Research: Biogeosciences, 113, 2008.

Garreaud, R., Clem, K., and Veloso, J. V.: The South Pacific pressure trend dipole and the southern blob, Journal of Climate, 34, 7661–7676, 2021.

Goulden, M. L. and Bales, R. C.: California forest die-off linked to multi-year deep soil drying in 2012–2015 drought, Nature Geoscience, 12, 632–637, 2019.

Gultepe, I. and Milbrandt, J.: Microphysical observations and mesoscale model simulation of a warm fog case during FRAM project, in: Fog and boundary layer clouds: Fog visibility and forecasting, pp. 1161–1178, Springer, 2007.

Gultepe, I., Heymsfield, A. J., Fernando, H., Pardyjak, E., Dorman, C., Wang, Q., Creegan, E., Hoch, S., Flagg, D., Yamaguchi, R., et al.: A review of coastal fog microphysics during C-FOG, Boundary-Layer Meteorology, 181, 227–265, 2021.

Keeley, J. E. and Syphard, A. D.: Large California wildfires: 2020 fires in historical context, Fire Ecology, 17, 1–11, 2021.

Kim, S., Rickard, C., Hernandez-Vazquez, J., and Fernandez, D.: Early Night Fog Prediction Using Liquid Water Content Measurement in the Monterey Bay Area, Atmosphere, 13, 1332, 2022.

Klemm, O., Schemenauer, R. S., Lummerich, A., Cereceda, P., Marzol, V., Corell, D., Van Heerden, J., Reinhard, D., Gherezghiher, T., Olivier, J., et al.: Fog as a fresh-water resource: overview and perspectives, Ambio, 41, 221–234, 2012.

Koch, M. A., Kleinpeter, D., Auer, E., Siegmund, A., del Rio, C., Osses, P., García, J.-L., Marzol, M. V., Zizka, G., and Kiefer, C.: Living at the dry limits: ecological genetics of Tillandsia landbeckii lomas in the Chilean Atacama Desert, Plant Systematics and Evolution, 305, 1041–1053, 2019.

Kogan, F. and Kogan, F.: Monitoring drought from space and food security, Remote sensing for food security, pp. 75–113, 2019.

Koppa, A., Keune, J., and Miralles, D. G.: Are Global Drylands Self-Expanding?, in: EGU General Assembly Conference Abstracts, pp. EGU–2320, 2023.

Larrain, H., Velásquez, F., Cereceda, P., Espejo, R., Pinto, R., Osses, P., and Schemenauer, R.: Fog measurements at the site "Falda Verde" north of Chañaral compared with other fog stations of Chile, Atmospheric Research, 64, 273–284, 2002.

Lobos-Roco, F., de Arellano, J. V.-G., and Pedruzo-Bagazgoitia, X.: Characterizing the influence of the marine stratocumulus cloud on the land fog at the Atacama Desert, Atmospheric research, 214, 109–120, 2018.

Lobos-Roco, F., Hartogensis, O., Vilà-Guerau de Arellano, J., De La Fuente, A., Muñoz, R., Rutllant, J., and Suárez, F.: Local evaporation controlled by regional atmospheric circulation in the Altiplano of the Atacama Desert, Atmospheric Chemistry and Physics Discussions, 2021, 1–38, 2021.

Lobos-Roco, F., Suárez, F., Aguirre-Correa, F., Keim, K., Aguirre, I., Vargas, C., Abarca, F., Ramírez, C., Escobar, R., Osses, P., et al.: Understanding inland fog and dew dynamics for assessing potential non-rainfall water use in the Atacama, Journal of Arid Environments, 221, 105 125, 2024.

Lu, M.-L., Conant, W. C., Jonsson, H. H., Varutbangkul, V., Flagan, R. C., and Seinfeld, J. H.: The marine stratus/stratocumulus experiment (MASE): Aerosol-cloud relationships in marine stratocumulus, Journal of Geophysical Research: Atmospheres, 112, 2007.

Malik, F., Clement, R., Gethin, D., Krawszik, W., and Parker, A.: Nature's moisture harvesters: a comparative review, Bioinspiration & biomimetics, 9, 031 002, 2014.

Masson-Delmotte, V., Zhai, P., Pirani, A., Connors, S. L., Péan, C., Berger, S., Caud, N., Chen, Y., Goldfarb, L., Gomis, M., et al.: Climate change 2021: the physical science basis, Contribution of working group I to the sixth assessment report of the intergovernmental panel on climate change, 2, 2391, 2021.

Moat, J., Orellana-Garcia, A., Tovar, C., Arakaki, M., Arana, C., Cano, A., Faundez, L., Gardner, M., Hechenleitner, P., Hepp, J., et al.: Seeing through the clouds–Mapping desert fog oasis ecosystems using 20 years of MODIS imagery over Peru and Chile, International Journal of Applied Earth Observation and Geoinformation, 103, 102 468, 2021.

Montecinos, S., Carvajal, D., Cereceda, P., and Concha, M.: Collection efficiency of fog events, Atmospheric research, 209, 163–169, 2018.

Muñoz, R. C., Zamora, R. A., and Rutllant, J. A.: The coastal boundary layer at the eastern margin of the southeast Pacific (23.4 S, 70.4 W): Cloudiness-conditioned climatology, Journal of climate, 24, 1013–1033, 2011.

630   Muñoz-Schick, M., Pinto, R., Mesa, A., and Moreira-Muñoz, A.: " Oasis de neblina" en los cerros costeros del sur de Iquique, región de
            Tarapacá, Chile, durante el evento El Niño 1997-1998, Revista chilena de historia natural, 74, 389–405, 2001.

       Painemal, D. and Zuidema, P.: Assessment of MODIS cloud effective radius and optical thickness retrievals over the Southeast Pacific with
            VOCALS-REx in situ measurements, Journal of Geophysical Research: Atmospheres, 116, 2011.

       Roach, W.: Back to basics: Fog: Part 2—The formation and dissipation of land fog, weather, 50, 7–11, 1995.

635   Schemenauer, R. S. and Cereceda, P.: A proposed standard fog collector for use in high-elevation regions, Journal of Applied Meteorology
            and Climatology, 33, 1313–1322, 1994.

       Schween, J. H., del Rio, C., García, J.-L., Osses, P., Westbrook, S., and Löhnert, U.: Life Cycle of Stratocumulus Clouds over one Year at
            the Coast of the Atacama Desert, Atmospheric Chemistry and Physics, 2022, 1–33, 2022.

       Stull, R. B.: An introduction to boundary layer meteorology, vol. 13, Springer Science & Business Media, 2012.

640   Verbrugghe, N. and Khan, A. Z.: Water harvesting through fog collectors: a review of conceptual, experimental and operational aspects,
            International Journal of Low-Carbon Technologies, 18, 392–403, 2023.

       Wetzel, P. J.: A simple parcel method for prediction of cumulus onset and area-averaged cloud amount over heterogeneous land surfaces,
            Journal of Applied Meteorology and Climatology, 29, 516–523, 1990.

       Wood, R.: Stratocumulus clouds, Monthly Weather Review, 140, 2373–2423, 2012.